Dimerization of assimilatory NADPH-dependent sulfite reductase reveals elements for diflavin reductase binding at a minimal interface

Behrouz Ghazi Esfahani[1], Nidhi Walia[1,2], Kasahun Neselu[3], Mahira Aragon[3], Isabel Askenasy[1,4], Alex Wei[3], Joshua H. Mendez[3], and M. Elizabeth Stroupe[1]

[1]Department of Biological Science and Institute of Molecular Biophysics, Florida State University, Tallahassee, FL, 32303, USA

[2]Current Location: Department of Biochemistry, Purdue University, West Lafayette, IN, 47907, USA

[3]New York Structural Biology Center, New York, NY, 10027, USA

[4]Current Location: Department of Biochemistry, University of Cambridge, Cambridge, CB2 1QW, UK

Corresponding Author: M. Elizabeth Stroupe
Address: Florida State University
91 Chieftain Way
Tallahassee, FL 32306
Phone: 850-645-1751
e-mail: mestroupe@bio.fsu.edu

Classification: Biological Sciences / Biochemistry

Keywords: NADPH-dependent assimilatory sulfite reductase; hemoflavoprotein; oxidoreductase; cryo-EM

Abstract
Escherichia coli NADPH-dependent assimilatory sulfite reductase is responsible for fixing sulfur for incorporation into sulfur-containing biomolecules. The oxidoreductase is composed of two subunits, an NADPH, FMN, and FAD-binding diflavin reductase and an iron siroheme and Fe_4S_4-containing oxidase. How they interact has been an unknown for over 50 years because the complex is highly flexible, thus has been intransigent for traditional X-ray or cryo-EM structural analysis. Using a combination of the chameleon plunging system with a fluorinated lipid we overcame the challenge of preserving the minimal dimer between the subunits for high-resolution cryo-EM analysis. Here, we report the first structure of the complex between the reductase and oxidase, revealing how they interact in a minimal interface. Further, we determined the structural elements that discriminate between the pairing of a siroheme-containing oxidase with a diflavin reductase or a ferredoxin partner to channel the six electrons that reduce sulfite to sulfide.

Significance Statement
Sulfur is one of the essential building blocks of life. Sulfur exists in numerous redox states but only one can be incorporated into biomass – S^{2-} (sulfide). In *Escherichia coli*, a protein enzyme called sulfite reductase reduces sulfite by six electrons to make sulfide. Typical electron transfer reactions move one or two electrons at a time, so this chemistry is unique. To do so, *E. coli* uses a two protein complex with unique co-enzymes. To date, how the subunits interact so the co-enzymes can transfer electrons has remained a mystery because the complex is structurally dynamic, thus difficult to analyze with traditional methods. This study shows for the first time the structure of the enzyme complex that performs this unique chemistry.

Introduction

Assimilatory sulfite reduction by NADPH-dependent sulfite reductase (SiR) is essential to produce sulfide for incorporation into sulfur-containing biomolecules. In γ-proteobacteria like *Escherichia coli*, SiR is a multimeric oxidoreductase composed of an octameric diflavin reductase (SiRFP) and four independently binding subunits of a siroheme-containing hemoprotein (SiRHP) (1-3).

The *E. coli* SiRFP subunit is homologous to cytochrome P450 (CYP) reductase (CPR) (4), the reductase domain of the bacterial CYP/CPR fusion CYP102A1/CYPBM3 (5), the reductase domain of nitric oxide synthase (NOSr) (6, 7), and methionine synthase reductase (MSR) (8). One of the hallmarks of this diflavin reductase family is that they are exceptionally conformationally malleable, which makes structural analysis challenging. For example, to date there are no high-resolution structures of the full-length NOS homodimer, the complex between methionine synthase and MSR, or the SiR heterododecameric holoenzyme (for simplicity, here referred to as a dodecamer). The structure of the CYP/CPR heterodimer and CYPBM3 are known (9-11), but CYP/CPR form a 1:1 heterodimer, whereas the oxidase and reductase domains are fused in CYPBM3, so little can be inferred about other homologs that function as higher-order protein complexes.

Despite its homology to other well-studied diflavin reductases, SiRFP is unique because it assembles into an octamer through its N-terminal 52 amino acids (12). Removing those amino acids results in a 60 kDa monomer (SiRFP-60), which binds SiRHP as a 1:1 heterodimer with reduced activity (3). Further, removing the complete N-terminal FMN-binding flavodoxin (Fld) domain results in a 43 kDa monomer that contains just the NADPH- and FAD-binding $NADP^+$ ferredoxin reductase (FNR) domain (SiRFP-43), which also binds SiRHP as a 1:1 heterodimer but is inactive for electron transfer (13) (Abbreviations and theoretical molecular weights are summarized in Table S1).

SiRHP has few known homologs because of its unique siroheme/Fe_4S_4 cluster assembly that form the sulfite-binding active site (14). Assimilatory SiRs or siroheme-dependent nitrite reductases (NiRs) from other bacterial species or plants have a similar hemoprotein but use a transiently bound ferredoxin as their electron source (15-17). SiRs that are responsible for energy conversion, dissimilatory sulfite reductases (DSRs), share a common siroheme binding fold but are heterotetrameric and are often fused to auxiliary domains (18). Their electron donors are poorly understood. Here, we show the first high-resolution cryogenic electron microscopy (cryo-EM) structure of the minimal SiRFP/SiRHP dimer, which elucidates their binding interface to understand how SiRHP tightly binds SiRFP's FNR domain.

Results

The SiRHP-SiRFP interaction is highly sensitive to cryogenic TEM (cryo-EM) preparation

We determined the structure of the SiRFP/SiRHP dimer from three modified, minimal dimers, each of which is named by the change to SiRFP and its resulting molecular weight (Table S1). First, we truncated SiRFP to remove the N-terminal Fld domain (SiRFP-43/SiRHP). This is an inactive dimer, as the Fld domain is required for electron transfer. Nevertheless, the two subunits bind tightly and is the most simplified complex between SiRFP and SiRHP (19). Second, we truncated both SiRFP's N-terminal octamerization domain as well as the linker between the Fld and FNR domains to create a monomeric SiRFP that can be locked in an open position (SiRFP-60Δ/SiRHP) (20). Third, we generated a variant of monomeric SiRFP-60 lacking reactive cysteines into which we engineered a disulfide bond between the Fld and FNR domains (SiRFP-60X/SiRHP) (21).

Each variant is highly sensitive to traditional blotting plunge-freezing methods for cryo-EM preservation. To overcome this sensitivity, we combined the protection of a high critical micelle concentration, fluorinated lipid, fos-choline-8 (FF8, Creative Biolabs, Shirley, NY, USA) (22), with the blot-free, rapid plunging afforded by the chameleon system (SPT Labtech, Melbourn, UK) (23). This cryo-EM sample preparation helped us to retain each intact complex within near ideal ice thickness and avoid denaturation at the air water interface (Fig. S1). The smallest complex (SiRFP-43/SiRHP) showed well-aligned 2D class averages, however the 3D structure revealed structural anisotropy, either due to its small size/asymmetric geometry or from a preferred orientation, that limited high-resolution analysis despite the absence of mobile elements (Figs. S1A and S2). SiRFP-60Δ/SiRHP showed moderate-resolution density (3.54 Å) for the SiRFP FNR domain and SiRHP, however the N-terminal Fld domain was not visible (Figs. S1B and S3A). The 2.84 Å-resolution structure of SiRFP-60X/SiRHP revealed the most detail for SiRFP's Fld and FNR domains, despite a lack of density for the linker between SiRFP's domains in the highest-resolution reconstruction (Figs. 1A, S1C, and S3B). High resolution features for each of the cofactors in both subunits supported this reported resolution (Fig. S4). Therefore, we analyzed the SiRFP-SiRHP interface for this construct in detail.

SiRFP-SiRHP binding

The SiR dodecameric holoenzyme is composed of oligomers of the dimers discussed here and is about 800 kDa in mass. Despite this large mass, the binding interface between the minimal SiRFP/SiRHP dimer is small, reaching the surface area of 1,138 $Å^2$ relative to the overall surface of 43,610 $Å^2$. SiRHP alone has a solvent-exposed surface of 25,680 $Å^2$. SiRFP-60X alone has a solvent-exposed surface of 21,930 $Å^2$. That is, for a large complex only about 2.6% of the solvent-exposed surface is buried upon subunit binding. This is consistent with hydrogen-deuterium exchange data on the complex that reveals single, short peptides from each subunit that become occluded upon binding (3), the sequences of which predicted the interface would be dominated by hydrophobic interactions (Fig. 1B).

The interface is governed by the N-terminus of SiRHP. The structure of this region is previously uncharacterized as it is proteolytically removed in the X-ray crystal structure of *E. coli* SiRHP (24). These 80 amino acids follow the topology helix 1 - loop - helix 2 - turn - helix 3 - β-strand 1 - helix 4 - loop - β-strand 2 (Fig. 1C). Only amino acids from the turn, helix 4, and surrounding loops directly interact with SiRFP. The regions that are N-terminal to the interface interact with domain 1 or the N-terminal half of the parachute domain (*i.e.* the first sulfite or nitrite reductase repeat (S/NiRR) (24, 25)), breaking SiRHP's pseudo two-fold symmetry (Figs. 1A and S5A). An extension to the parachute domain that is not ordered in the original crystal structure, from amino acids 184-209, helps to hold the N-terminus in place (Fig. S5A). Those that are N-terminal to the interface approach the distal active site, but do not contribute significantly to anion or siroheme binding as they are held back by interactions to SiRFP, discussed below. Moving N-terminally along the peptide, it then turns back to form the loop that binds a pocket in SiRFP before moving away from SiRFP. The N-terminal most amino acids reach all the way to the other side of SiRHP, interacting with the N-terminus of the α-helix (h11) that precedes the linker that joins the two S/NiRRs and mimics the siroheme binding site (Fig. S5B) (24).

The central interaction that pegs the subunits together is a π-cation interaction between h-Lys27 from SiRHP (for simplicity, amino acids from SiRHP will be designated with the prefix "h-") and f-His258 from SiRFP (similarly, amino acids from SiRFP will be designated with the prefix "f-") (Figs. 1D and E). This interaction is buttressed by f-Phe496 and f-Val500, which have previously been shown essential for SiRFP-SiRHP binding (13). Further hydrophobic and π-stacking interactions dominate the interface. For example, h-Leu40 inserts into a pocket in SiRFP formed between f-

β-sheet 17 and f-α-helix 18, which includes f-Phe496. h-Ile65 Cγ2 sits 3.3 Å from the plane of f-Arg250's guanidinium group (Figs. 1D and F), which is rotated 90° from its position in free SiRFP (20). h-Gln72Cγ also packs into a pocket formed by the backbone atoms of f-Ile247, f-Thr248, and f-Gly249, pinned in place by the h-Ile65/f-Arg250 and h-Lys73/f-His258 interactions. Farther from the interface, there is another stacking interaction between the guanidinium group from h-Arg63 and the h-Phe437 aromatic ring that stabilized the deformed helix that includes h-Ile65 (Figs. 1D and G). h-Phe437 is adjacent, through h-A443, to SiRHP's iron-sulfur cluster. In this way, the binding interface between SiRFP and SiRHP reaches to the SiRHP active site through a network of hydrophobic interactions (Fig. S6).

Neither ionic interactions nor hydrogen bonds play a direct role in the interface, but rather stabilize the amino acids and structural elements that mediate the interface (Figs. 1C, D and S6). For example, a hydrogen bond network from f-Thr404Oγ through f-Tyr498OH and finally to f-His258Nδ1 position its imidazole ring for the interaction with h-Lys73. An ionic interaction between h-Lys127Nζ and h-Asp38Oδ2 reach across the loop, presenting h-Leu40 to project into SiRFP's pocket. An additional ionic interaction between h-Asp61δ1 and h-Arg66NHδ also stabilize the deformed helix that contains h-Ile65 and turn it towards f-Arg250.

The SiRHP interaction with SiRFP differs from SIR interaction with ferredoxin

γ-proteobacteria couple a diflavin reductase, SiRFP, to SiRHP. In contrast, other organisms like *Zea mays* and *Mycobacteria tuberculosis* use a ferredoxin (Fd) as their reductase partner (15, 17). In *Z. mays* SIR, Fd bridges SIR's C-terminal domain 2 to a loop between the first two β-strands (amino acids Asp110 to Asn118), positioning the Fd iron-sulfur cluster near the SIR metal sites (26). The interaction is bolstered by *en face* stacking between Fd Tyr37 and SIR Arg324 (Fig. 2A).

In SiRHP, the equivalent element between the structurally conserved β-strands 1 and 2 is considerably longer, stretching from h-Asp62 to h-Arg77 and containing a short helix from h-Arg63 to h-Glu71 (Fig. 2B). This loop contains the critical residues h-Gln72 and h-Lys73 that anchor the interaction with SiRFP's FNR domain, which faces away from where Fd binds to the *Z. mays* homolog (Fig. 2C). Further, the arginine in SIR that stacks with Fd Tyr37 is not conserved in SiRHP – the equivalent position is h-Gly262, despite the structural conservation of the loop between β-strands 7 and 8 that contributes to siroheme binding (Fig. 2D).

The SiRHP active site loop is locked in its closed conformation

When bound to SiRFP, SiRHP's anion binding loop (h-Asn149 to h-Arg153) is in its closed position, held in place by a long, through-space interaction between h-Arg53 and h-Asn149 (Fig. 3A). h-Arg53 is, in turn, held in place by stacking between its guanidinium group and h-Tyr58. The ring of h-Tyr58 subsequently sits over the methyl group on the siroheme pyrroline A ring. The only other new protein/siroheme interaction identified in this now complete structure of SiRHP is an ionic bond between h-Gln60 and the propionyl group from siroheme pyrroline ring B. The siroheme is saddle-shaped, as in free SiRHP and unlike in dissimilatory SIR (27-30). h-Arg153 is flipped away from the bound phosphate. The other three anion binding amino acids, h-Arg83, h-Lys215, and h-Lys217, remain largely unchanged from free SiRHP (Figs. 3A-C) (24).

This conformation differs from the various redox and anion-bound structures of free SiRHP (24, 31-33). In the phosphate-bound, free SiRHP structure that lacks the N-terminal 80 amino acid extension (24), the loop is flipped open such that h-Ala146-h-Ala148 are disordered (Fig. 3B). Upon reduction and sulfite binding, h-Arg153 flips over to interact with the smaller anion and the loop becomes ordered (32). h-Asn149 points away from the active site. In this way, SiRFP binding

to SiRHP, with the ordering of SiRHP's N-terminus, induces an intermediate structure with elements of both the oxidized, phosphate bound and the reduced, sulfite bound conformations (Fig. 3D).

In the original SiRHP X-ray crystal structure, the siroheme iron is significantly domed above the siroheme nitrogens, indicative of an oxidized Fe^{3+} (Fig. 3B) (24). Subsequent chemical reduction experiments show the doming flattens upon conversion to Fe^{2+}, commensurate with release of the phosphate to allow substrate binding (Fig. 3B) (32). Contemporary X-ray diffraction experiments show that this reduction is beam-induced, but within the constraints of the crystal the phosphate remains bound to the siroheme iron in the active site (33). In this cryo-EM structure, the siroheme iron appears to be in the plane of the siroheme nitrogens, suggesting that it has also been reduced by the electron beam. The central density for the phosphate is 3.5 Å from the siroheme iron and its pyramidal shape is rotated such that the oxygen-iron bond is broken (Figs. 3A and S4C).

SiRFP is highly mobile

Although the 2D class averages in all three datasets appeared to show little orientation preference with discernable features, further analysis revealed each to have unique properties related to the SiRFP variant used to generate the dimer (Table S1, Figs. S1-3).

SiRFP-43/SiRHP (107 kDa in mass): The 2D class averages for SiRFP-43/SiRHP appeared to show high-resolution features, however the initial 3D models were poorly aligned, likely due to a combination of small mass, preferred orientation, and limitations in grid preparation, so the refined volume did not achieve high resolution despite its simplified form. 3D variability analysis in CryoSPARC (34) did not reveal significant conformational mobility, however orientation analysis and calculation of the 3DFSC (35) showed the particles harbored a preferred orientation (Fig. S2). Nevertheless, the absence of SiRFP's Fld domain did not alter the SiRFP-SiRHP interaction.

SiRFP-60Δ/SiRHP (123 kDa): As with SiRFP-43/SiRHP, this dimer showed 2D class averages with high-resolution features for the core of the dimer (Figs. S1B and S3A). Nevertheless, the initial models were of inconsistent structure, so we checked for heterogeneity using "3D variability" in CryoSPARC, which revealed a distinctive degree of movement in the Fld domain. To better understand the degree of flexibility for the Fld domain from the SiRFP-60Δ/SiRHP dimer, we performed both "3D flex" in CryoSPARC as well as "heterogenous refinement" in cryoDRGN (36) with the particles from refinement on the main heterodimer body. This analysis, anchored on the SiRFP-FNR/SiRHP dimer, identified a dramatic movement of SiRFP's Fld domain relative to the FNR domain, swinging 20° between the most compact and most open forms (Video S1 and Fig. 4A). The density for the linker joining the domains is not visible. In its most compact conformation, the Fld domain reaches the canonical "closed" conformation in which the Fld domain tucks into a cavity in the FNR domain (Fig. 4B). In the most open conformation, the Fld domain assumes a different position to that seen in the "open" conformation determined by X-ray crystallography of the same monomeric variant and the average solution envelope determined from SANS, intermediate between the fully opened and closed conformations (Fig. 4C) (19, 20).

SiRFP-60X/SiRHP (124 kDa): The Fld and FNR domains are covalently linked in this dimer, thus restricting the swinging domain motion of the Fld domain seen in the SiRFP-60Δ/SiRHP dimer. No preferred orientation was identified either in 2D or 3D analysis (Fig. S3B). Nevertheless, there is no density for the linker between the Fld and FNR domains in the highest-resolution reconstruction, which suggests that the 36 amino acid linker is exceptionally dynamic but allows SiRFP's two domains to come into close contact to catch them in a crosslink. Locking the Fld and

FNR domains in the closed conformation resulted in the most stable variant for high-resolution analysis (2.84 Å), discussed above.

With further classification of the SiRFP-60X/SiRHP structure, a sub-class of ~20,000 particles (10% of the particles used for highest resolution reconstruction for this dataset) emerged that revealed the linker between the two domains. The linker runs from the C-terminal end of the Fld domain (amino acid f-Ser207) to the N-terminal end of the FNR domain (amino acid f-Ile226) (Fig. 4D). There is neither defined secondary structure nor contact with either of the SiRFP domains, thus the linker is not constrained in a single conformation across the entire ensemble of particles even when the domains are crosslinked. The highly mobile nature of these 36 amino acids explains how the Fld domain can reposition for contact with the oxidase partner, SiRHP, presumably to mediate electron transfer.

Discussion

The interface between the SiRHP and SiRFP subunits of the SiR holoenzyme is surprisingly minimal, driven by π-cation, hydrophobic, and planar stacking between aromatic amino acids. The non-canonical planar stacking interactions with strategic arginine residues are not as uncommon as would be expected from the canonical role that arginine plays in electrostatic interactions and are often found at important structural elements of the protein or enzyme (37). In the case of the SiRFP/SiRHP dimer, these interactions either mediate the dimer interface itself or establish the structural platform for other amino acids to mediate the interface. Polar or electrostatic interactions play supporting roles to align the non-polar interactions because the arginine amino groups are free to make independent, more canonical, interactions with other side chains.

The curious combination of non-ionic interactions that holds the complex together explains why cryo-EM analysis has been elusive – the hydrophobic air-water interface in a thin film for cryogenic plunging is destructive for such interactions (38-41). We performed extensive trial-and-error probing grid type, grid substrate, hole size, method for hydrophilizing the grid, detergents, and plunging methods to identify what seems to be a singular condition that allowed cryogenic preservation for cryo-EM analysis: the combination of FF8 and the chameleon blot-free, rapid plunging. Neither FF8 alone with traditional plunging nor chameleon alone without FF8 was sufficient. Such low-throughput screening to find the one combination of variables that allows for high-quality sample preparation highlights the need for further technology development on the front-end of cryo-EM structure determination. High-throughput data collection with direct electron detectors is not sufficient to overcome cryo-EM sample preparation challenges.

Surprisingly minimal structural elements determine the evolutionary pressure for siroheme-dependent SiR oxidases to partner with a diflavin reductase like SiRFP or a simpler Fd reductase. For example, in comparing the only known structures of monomeric assimilatory SiR oxidases with their reductase partners – *E. coli* SiRHP (this work) and *Z. mays* SIR (26) – a single loop extension between a core two-strand β-sheet discriminates between Fd binding in the case of *Z. mays* SIR and the binding of SiRHP to the FNR domain of SiRFP in the case of *E. coli*. *E. coli* has only one *fdx* gene that does not fulfill the reductase function for SiRHP, given that strains of *E. coli* lacking the gene encoding SiRFP (*cysJ*) cannot grow in a low sulfur environment (14).

The SiRFP/SiRHP dimeric structure reported here shows that when SiRHP binds SiRFP, the anion-binding active site loop is locked in its closed conformation, constrained from disorder. Nevertheless, h-Arg153 is in its phosphate-binding conformation. The position of the loop is, thus, impacted by the presence of SiRHP's N-terminus that is absent in the X-ray crystal structure. The importance of this observation is understood in comparison to a series of X-ray crystal structures in various redox states and bound to various anions (31, 32). This series of structures shows how

the active site re-orients with the changing state, namely that the loop between h-Asn149 to h-Arg153 is disordered in the oxidized state. Upon reduction the loop becomes ordered and h-Arg153 flips to bind the substrate.

The question that remains is how SiRFP's Fld domain approaches SiRHP's metallic active site for productive electron transfer as it does not mediate the structural interaction between the subunits. Clearly there is dramatic flexibility within SiRFP, even when the Fld and FNR domains are covalently attached by an engineered crosslink – we cannot visualize the linker between the domains without extensive classification. Within this minimal dimer, the crosslink is intramolecular but in the SiR dodecameric holoenzyme, we have observed both intermolecular and intramolecular crosslinks (21). Further, despite our extensive efforts at determining the structure of the full complex, the dodecamer has proven to be highly heterogeneous. Together, these observations support the hypothesis that within the holoenzyme, there is not a singular inter-subunit interaction between the Fld and FNR domains of any given SiRFP subunit within the octamer.

The basis for SiRFP's extreme flexibility is that the linker between the Fld and FNR domains is 36 amino acids long, compared to the 12 amino acid long linker in CPR (42). Heterogeneity analysis of SiRFP-Δ in complex with SiRHP identified a dominant vector of motion parallel to the major axis of the FNR domain. This is in contrast to the highly extended conformation seen in the X-ray crystal structure of free SiRFP-Δ (20). In this way, there is not a single axis along which the Fld domain moves relative to the FNR domain such that the Fld domain makes a productive interaction with SiRHP within a SiRHP/SiRFP dimer. Nevertheless, prior biochemical experimentation shows that cross-subunit interactions occur within the SiRFP octamer (21). Thus, it is likely that a unique, single electron transfer-pathway does not exist within the full, dodecameric holoenzyme complex.

Conclusions

The combined technological developments in cryo-EM over the past decade all played a role in determining the structure of this elusive complex, from cryogenic sample preservation to data collection to image analysis. In doing so, we show that the subunits of NADPH-dependent assimilatory sulfite reductase bind through an interface governed by the N-terminus of SiRHP and the FNR domain of SiRFP. The interaction is surprisingly minimal, governed by a set of hydrophobic and stacking interactions. Structural pairing between a siroheme-dependent oxidase and diflavin reductase or ferredoxin appears to fall to a short loop between a conserved 2-stranded β sheet. The high mobility of SiRFP's Fld domain relative to its FNR domain likely explains how a minimal dimer maintains redox-dependent functionality and provides a mechanism for redundant electron transfer pathways within the dodecamer that efficiently performs the six-electron reduction of sulfite to sulfide.

Materials and methods

Protein Expression and Purification

Each SiRFP/SiRHP dimer variant was generated and purified as previously described (2, 3, 13, 19, 21). Briefly, untagged SiRHP was co-purified with the following SiRFP variants: 1) SiRFP-43, a 43 kDa monomeric SiRFP variant lacking the N-terminal Fld domain and linker (19); 2) SiRFP-60Δ, a 60 kDa monomeric variant of SiRFP generated by truncating its first 52 amino acids with an additional internal truncation of six amino acid (Δ-AAPSQS) in the linker that joins the Fld and FNR domains (20); and 3) SiRFP-60X, the 60 kDa monomer with an engineered disulfide crosslink between the Fld and FNR domains, as has previously been analyzed in octameric SiRFP (21). In SiRFP-60X, two background cysteines (C162T and C552S) were altered to avoid

unwanted crosslinking and two cysteines were added (E121C and N556C) to form a disulfide bond between Fld and FNR domains of SiRFP, previously confirmed by mass spectroscopy analysis (21). DNA sequencing confirmed the presence of all deletions and mutations in the variants.

E. coli LMG194 cells (Invitrogen, Carlsbad, CA, USA) were transformed with the pBAD plasmid containing the genes encoding SiRFP-60Δ, SiRFP-60X, SiRFP-43 or SiRHP. All variants were expressed independently. Dimers were formed as followed: for SiRFP-43/SiRHP and SiRFP-60Δ/SiRHP, cells were mixed before lysis and the dimers co-purified. The SiRFP-60X/SiRHP dimer was assembled by reconstituting SiRFP-60X with 2 Eq SiRHP for 1 h on ice, as before (2, 19, 21). A six-histidine tag was present in all SiRFP variants whereas SiRHP was untagged. Each recombinant *E. coli* strain was grown and induced at 25 °C with 0.05% L-arabinose. SiRFP-43, SiRFP-60Δ and SiRHP cells were expressed for 4 hr whereas SiRFP-60X was expressed overnight. All variants were purified using a combination of Ni-NTA affinity chromatography (Cytiva, Marlborough, MA, USA), anion exchange HiTrap-Q HP chromatography (Cytiva, Marlborough, MA, USA) and Sephacryl S300-HR size exclusion chromatography (Cytiva, Marlborough, MA, USA) using previously optimized SPG buffers (17 mM succinic acid, 574 mM sodium dihydrogen phosphate, pH 6.8, 374 mM glycine, 200 mM NaCl) (2, 13, 19, 21). All variants have been extensively characterized with UV-Vis spectroscopy, size exclusion chromatography, SDS PAGE analysis for correct stoichiometry and with SANS for solution monodispersity (Fig. S7) (2, 13, 19, 21).

Cryo-EM sample preparation

SiRFP-43/SiRHP, SiRFP-60Δ/SiRHP and SiRFP-60X/SiRHP were all plunged using the chameleon blotless plunging system (SPT Labtech, Melbourn, UK) at 10 mg/mL protein. chameleon self-wicking grids (23) were backed with 18-gauge gold (Ted Pella, Redding CA, USA) on an Auto 306 vacuum coater (BOC Edwards, West Sussex, UK). The following glow discharge (GD)/wicking times (WTs) were used: SiRFP-43/SiRHP: 30 s GD, 130 ms WT; SiRFP-60Δ/SiRHP: 80 s GD, 195 ms WTs; SiRFP-60X/SiRHP 45 s GD, 175 ms WTs. All samples were premixed with FC-8 detergent (22) at 2 mM final concentration. The plunged grids were clipped and then screened for high quality with a Titan Krios operating the Leginon software package (43).

Data collection and processing

1) SiRFP-43/SiRHP: 14,600 movies were collected at 300 KV on a Titan Krios using a GATAN K3 camera with 0.844 Å/pixel. After motion correction with Motioncor2 (44) in the Relion GUI (45), CTF estimation was performed using CTFFIND4 (46). Particles were picked by “blob picker” followed by “template picker” in CryoSPARC (34). Initial 2D classification, followed by multiple rounds of 2D class selection/classification, identified 1,500,000 particles that were used for initial map building and non-uniform refinement in CryoSPARC. This process achieved a reported 3.6 Å-resolution map of the minimal dimer. However, the map features did not reflect the reported resolution. “Orientation diagnostic” job from CryoSPARC was performed to confirm this interpretation. To further confirm and diminish the preferred orientation issue, “Rebalance 2D” was performed to put particles into 7 super classes and limit the total particles in each superclass down to total of 350,000 and 105,000 particles. Non-uniform refinement (47) followed by orientation diagnostics performed in CryoSPARC produced a more accurate resolution (4.31 Å, 4.74 Å respectively) and better quality map. deepEMhancer (48) was used to sharpen these

maps (Fig. S2). Particle picking performed by the TOPAZ algorithm (49) gave the same result.

2) SiRFP-60Δ/SiRHP: 25,488 movies were collected at 300 KV on a Titan Krios using a GATAN K3 camera with 0.844 Å/pixel. Motion correction, CTF estimation, and particle picking were performed as for SiRFP-43/SiRHP. After multiple rounds of 2D classification, ~550,000 particles were used for initial map building and non-uniform refinement in CryoSPARC to achieve the final 3.49 Å-resolution structure of the dimer, masked to omit SiRFP's Fld domain. Multiple refinements with different masking were performed. Masking to include the whole complex, including SiRFP's Fld domain, resulted in a low resolution reconstruction for the Fld domain. Particles were then down sampled and imported to cryoDRGN to perform heterogenous refinement, giving a series of volumes showing the Fld domain movement. CryoSPARC 3D Flex (50) gave the same result as cryoDRGN.
3) SiRFP-60X/SiRHP: ~10,000 movies were collected at 300 KV on a Titan Krios using a DE Apollo camera with 0.765 Å/pixel. Motion correction, CTF estimation, and particle picking were performed as above. Multiple rounds of 2D classifications identified ~185,000 particles that were used for initial map building and non-uniform refinement in CryoSPARC to achieve a 2.84 Å-resolution structure of the entire dimer, including SiRFP's Fld domain. Further 3D variability was performed to track the Fld linker. After multiple rounds of 3D classification 10% of the particles (~20,000) were used to perform a non-uniform refinement, resulted in a 3.61 Å overall resolution structure, sharpened by deepEMhancer including the linker.

Model building and refinement.
Model building was initiated using the "fit in map" algorithm in Chimera (51) using the atomic model of SiRFP from PDB ID 6EFV (20), fitting each of the Fld or FNR domains independently or the atomic model of SiRHP generated in AlphaFold (52, 53) to capture its N-terminal 80 amino acids. Iterative real-space refinement in PHENIX (54) with manual fitting in Coot (55) yielded a model with a correlation of 0.85 (Table S3). The model deposited in PDB as 9C91and the map deposited in EMDB as EMD-45359.

Author contributions
BGE participated in data collection and performed the data analysis. NW and BGE prepared the protein specimen. KN and MA prepared cryogenic specimen and participated in data collection. IA optimized protein specimen preparation. AW and JHM supervised cryogenic specimen preparation and data collection. MES conceived of the study and oversaw experimentation.

Acknowledgements and funding
We kindly thank Dr.s Scott Stagg and Christopher Stroupe for helpful discussions. Some of this work was performed at the Simons Electron Microscopy Center at the New York Structural Biology Center, with major support from the Simons Foundation (SF349247). Florida State University supports cryo-EM in the Biological Imaging Resource Center, which houses the following equipment used in this study: a Gatan Solaris Plasma Cleaner (NIH grant S10 RR024564), a Hitachi HT7800 (NSF grant 2017869), a ThermoFisher Vitrobot Mark IV (NIH grant S10 RR024564), an SPI chameleon plunging system (NIH grant R24 GM145964), a ThermoFisher Titan Krios (NIH grant S10 RR025080), and a DE Apollo direct electron detector (NIH grant R35 GM139616). This work was further supported by National Science Foundation grants MCB1856502 and CHE1904612 to M.E.S.

References

1. L. M. Siegel, P. S. Davis, Reduced nicotinamide adenine dinucleotide phosphate-sulfite reductase of enterobacteria. IV. The Escherichia coli hemoflavoprotein: subunit structure and dissociation into hemoprotein and flavoprotein components. *J Biol Chem* **249**, 1587-1598 (1974).
2. D. T. Murray *et al.*, Neutron scattering maps the higher-order assembly of NADPH-dependent assimilatory sulfite reductase. *Biophys J* **121**, 1799-1812 (2022).
3. I. Askenasy *et al.*, The N-terminal Domain of Escherichia coli Assimilatory NADPH-Sulfite Reductase Hemoprotein Is an Oligomerization Domain That Mediates Holoenzyme Assembly. *J Biol Chem* **290**, 19319-19333 (2015).
4. M. Wang *et al.*, Three-dimensional structure of NADPH-cytochrome P450 reductase: prototype for FMN- and FAD-containing enzymes. *Proc Natl Acad Sci U S A* **94**, 8411-8416 (1997).
5. H. M. Girvan *et al.*, Flavocytochrome P450 BM3 and the origin of CYP102 fusion species. *Biochem Soc Trans* **34**, 1173-1177 (2006).
6. E. D. Garcin *et al.*, Structural basis for isozyme-specific regulation of electron transfer in nitric-oxide synthase. *J Biol Chem* **279**, 37918-37927 (2004).
7. J. Zhang *et al.*, Crystal structure of the FAD/NADPH-binding domain of rat neuronal nitric-oxide synthase. Comparisons with NADPH-cytochrome P450 oxidoreductase. *J Biol Chem* **276**, 37506-37513 (2001).
8. H. Olteanu, R. Banerjee, Human methionine synthase reductase, a soluble P-450 reductase-like dual flavoprotein, is sufficient for NADPH-dependent methionine synthase activation. *J Biol Chem* **276**, 35558-35563 (2001).
9. S. L. Freeman *et al.*, Solution structure of the cytochrome P450 reductase-cytochrome. *J Biol Chem* **293**, 5210-5219 (2018).
10. L. Zhang *et al.*, Structural insight into the electron transfer pathway of a self-sufficient P450 monooxygenase. *Nat Commun* **11**, 2676 (2020).
11. H. Zhang *et al.*, The full-length cytochrome P450 enzyme CYP102A1 dimerizes at its reductase domains and has flexible heme domains for efficient catalysis. *J Biol Chem* **293**, 7727-7736 (2018).
12. M. Zeghouf, M. Fontecave, J. Coves, A simplifed functional version of the Escherichia coli sulfite reductase. *J Biol Chem* **275**, 37651-37656 (2000).
13. I. Askenasy *et al.*, Structure-Function Relationships in the Oligomeric NADPH-Dependent Assimilatory Sulfite Reductase. *Biochemistry* **57**, 3764-3772 (2018).
14. L. M. Siegel, M. J. Murphy, H. Kamin, Reduced nicotinamide adenine dinucleotide phosphate-sulfite reductase of enterobacteria. I. The Escherichia coli hemoflavoprotein: molecular parameters and prosthetic groups. *J Biol Chem* **248**, 251-264 (1973).
15. M. Nakayama, T. Akashi, T. Hase, Plant sulfite reductase: molecular structure, catalytic function and interaction with ferredoxin. *J Inorg Biochem* **82**, 27-32 (2000).
16. R. Schnell, T. Sandalova, U. Hellman, Y. Lindqvist, G. Schneider, Siroheme- and [Fe4-S4]-dependent NirA from Mycobacterium tuberculosis is a sulfite reductase with a covalent Cys-Tyr bond in the active site. *J Biol Chem* **280**, 27319-27328 (2005).
17. R. Pinto, J. S. Harrison, T. Hsu, W. R. Jacobs, Jr., T. S. Leyh, Sulfite reduction in mycobacteria. *J Bacteriol* **189**, 6714-6722 (2007).
18. M. Jespersen, A. J. Pierik, T. Wagner, Structures of the sulfite detoxifying F 420-dependent enzyme from Methanococcales. *Nat Chem Biol* **19**, 695-702 (2023).
19. D. T. Murray, K. L. Weiss, C. B. Stanley, G. Nagy, M. E. Stroupe, Small-angle neutron scattering solution structures of NADPH-dependent sulfite reductase. *J Struct Biol* **213**, 107724 (2021).

20. A. M. Tavolieri *et al.*, NADPH-dependent sulfite reductase flavoprotein adopts an extended conformation unique to this diflavin reductase. *J Struct Biol* (2019).
21. N. Walia *et al.*, Domain crossover in the reductase subunit of NADPH-dependent assimilatory sulfite reductase. *J Struct Biol* **215**, 108028 (2023).
22. D. Kampjut, J. Steiner, L. A. Sazanov, Cryo-EM grid optimization for membrane proteins. *iScience* **24**, 102139 (2021).
23. T. S. Levitz *et al.*, Approaches to Using the Chameleon: Robust, Automated, Fast-Plunge cryoEM Specimen Preparation. *Front Mol Biosci* **9**, 903148 (2022).
24. B. R. Crane, L. M. Siegel, E. D. Getzoff, Sulfite reductase structure at 1.6 A: evolution and catalysis for reduction of inorganic anions. *Science* **270**, 59-67 (1995).
25. B. R. Crane, E. D. Getzoff, The relationship between structure and function for the sulfite reductases. *Curr Opin Struct Biol* **6**, 744-756 (1996).
26. J. Y. Kim, M. Nakayama, H. Toyota, G. Kurisu, T. Hase, Structural and mutational studies of an electron transfer complex of maize sulfite reductase and ferredoxin. *J Biochem* (2016).
27. T. F. Oliveira *et al.*, The crystal structure of Desulfovibrio vulgaris dissimilatory sulfite reductase bound to DsrC provides novel insights into the mechanism of sulfate respiration. *J Biol Chem* **283**, 34141-34149 (2008).
28. T. F. Oliveira *et al.*, Structural insights into dissimilatory sulfite reductases: structure of desulforubidin from desulfomicrobium norvegicum. *Front Microbiol* **2**, 71 (2011).
29. K. Parey, E. Warkentin, P. M. Kroneck, U. Ermler, Reaction cycle of the dissimilatory sulfite reductase from Archaeoglobus fulgidus. *Biochemistry* **49**, 8912-8921 (2010).
30. A. Schiffer *et al.*, Structure of the dissimilatory sulfite reductase from the hyperthermophilic archaeon Archaeoglobus fulgidus. *J Mol Biol* **379**, 1063-1074 (2008).
31. B. R. Crane, L. M. Siegel, E. D. Getzoff, Probing the catalytic mechanism of sulfite reductase by X-ray crystallography: structures of the Escherichia coli hemoprotein in complex with substrates, inhibitors, intermediates, and products. *Biochemistry* **36**, 12120-12137 (1997).
32. B. R. Crane, L. M. Siegel, E. D. Getzoff, Structures of the siroheme- and Fe4S4-containing active center of sulfite reductase in different states of oxidation: heme activation via reduction-gated exogenous ligand exchange. *Biochemistry* **36**, 12101-12119 (1997).
33. K. W. Smith, M. E. Stroupe, Mutational analysis of sulfite reductase hemoprotein reveals the mechanism for coordinated electron and proton transfer. *Biochemistry* **51**, 9857-9868 (2012).
34. A. Punjani, J. L. Rubinstein, D. J. Fleet, M. A. Brubaker, cryoSPARC: algorithms for rapid unsupervised cryo-EM structure determination. *Nat Methods* **14**, 290-296 (2017).
35. S. Aiyer, C. Zhang, P. R. Baldwin, D. Lyumkis, Evaluating Local and Directional Resolution of Cryo-EM Density Maps. *Methods Mol Biol* **2215**, 161-187 (2021).
36. E. D. Zhong, T. Bepler, B. Berger, J. H. Davis, CryoDRGN: reconstruction of heterogeneous cryo-EM structures using neural networks. *Nat Methods* **18**, 176-185 (2021).
37. M. M. Flocco, S. L. Mowbray, Planar stacking interactions of arginine and aromatic side-chains in proteins. *J Mol Biol* **235**, 709-717 (1994).
38. E. D'Imprima *et al.*, Protein denaturation at the air-water interface and how to prevent it. *Elife* **8** (2019).
39. R. M. Glaeser *et al.*, Factors that Influence the Formation and Stability of Thin, Cryo-EM Specimens. *Biophys J* **110**, 749-755 (2016).
40. R. M. Glaeser, B. G. Han, Opinion: hazards faced by macromolecules when confined to thin aqueous films. *Biophys Rep* **3**, 1-7 (2017).

41. R. M. Glaeser, PROTEINS, INTERFACES, AND CRYO-EM GRIDS. *Curr Opin Colloid Interface Sci* **34**, 1-8 (2018).
42. C. Xia *et al.*, Conformational changes of NADPH-cytochrome P450 oxidoreductase are essential for catalysis and cofactor binding. *J Biol Chem* **286**, 16246-16260 (2011).
43. C. Suloway *et al.*, Automated molecular microscopy: the new Leginon system. *J Struct Biol* **151**, 41-60 (2005).
44. S. Q. Zheng *et al.*, MotionCor2: anisotropic correction of beam-induced motion for improved cryo-electron microscopy. *Nat Methods* **14**, 331-332 (2017).
45. S. H. Scheres, RELION: implementation of a Bayesian approach to cryo-EM structure determination. *J Struct Biol* **180**, 519-530 (2012).
46. A. Rohou, N. Grigorieff, CTFFIND4: Fast and accurate defocus estimation from electron micrographs. *J Struct Biol* **192**, 216-221 (2015).
47. A. Punjani, H. Zhang, D. J. Fleet, Non-uniform refinement: adaptive regularization improves single-particle cryo-EM reconstruction. *Nat Methods* **17**, 1214-1221 (2020).
48. R. Sanchez-Garcia *et al.*, DeepEMhancer: a deep learning solution for cryo-EM volume post-processing. *Commun Biol* **4**, 874 (2021).
49. T. Bepler *et al.*, Positive-unlabeled convolutional neural networks for particle picking in cryo-electron micrographs. *Nat Methods* **16**, 1153-1160 (2019).
50. A. Punjani, D. Fleet, 3D Flexible Refinement: Determining Structure and Motion of Flexible Proteins from Cryo-EM. *Microsc Microanal* **29**, 1024 (2023).
51. E. F. Pettersen *et al.*, UCSF Chimera - A visualization system for exploratory research and analysis. *Journal of Computational Chemistry* **25**, 1605-1612 (2004).
52. J. Jumper *et al.*, Highly accurate protein structure prediction with AlphaFold. *Nature* **596**, 583-589 (2021).
53. J. P. Roney, S. Ovchinnikov, State-of-the-Art Estimation of Protein Model Accuracy Using AlphaFold. *Phys Rev Lett* **129**, 238101 (2022).
54. P. D. Adams *et al.*, PHENIX: a comprehensive Python-based system for macromolecular structure solution. *Acta Crystallogr D Biol Crystallogr* **66**, 213-221 (2010).
55. P. Emsley, B. Lohkamp, W. G. Scott, K. Cowtan, Features and development of Coot. *Acta Crystallogr D Biol Crystallogr* **66**, 486-501 (2010).

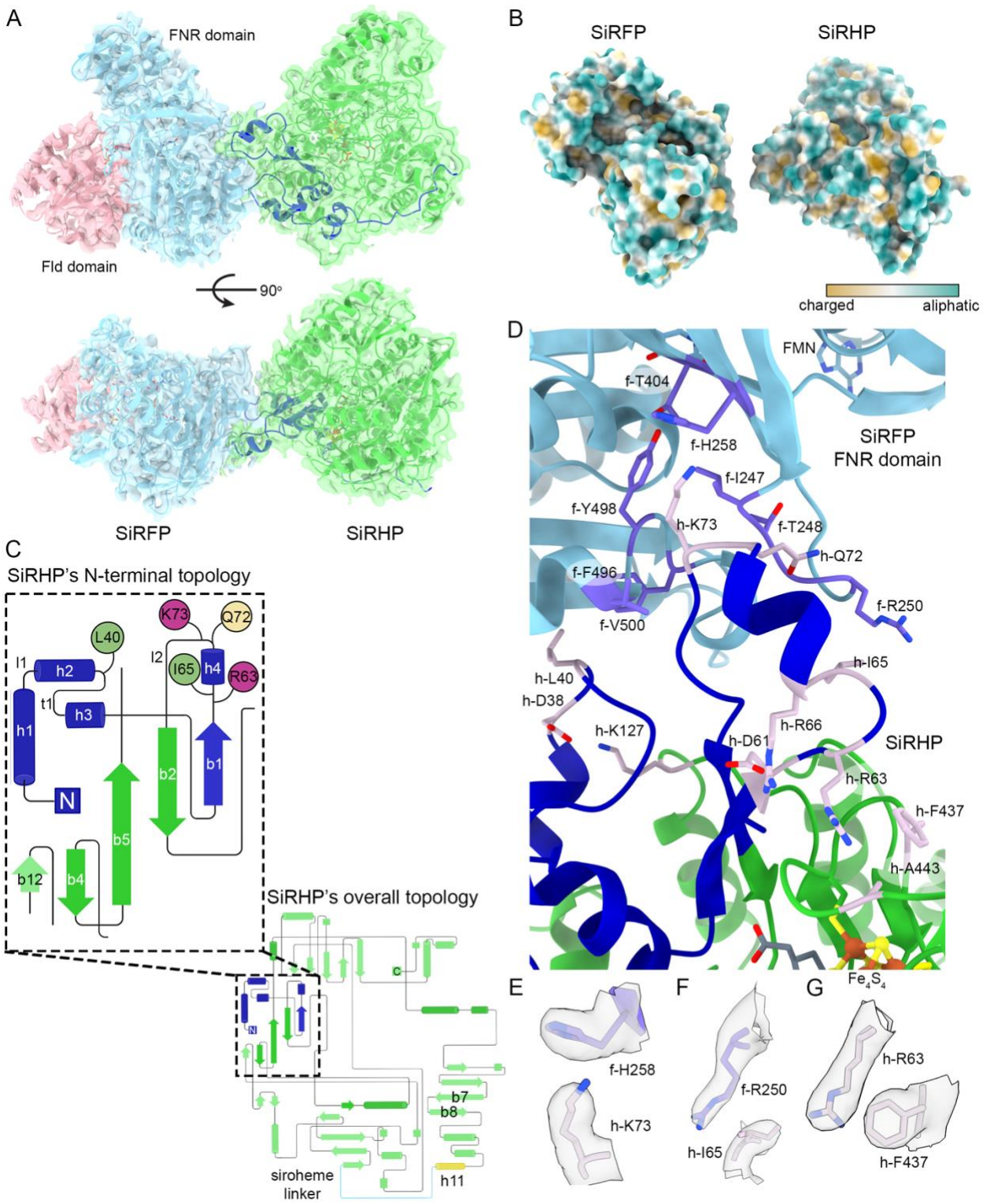
A
FNR domain
Fld domain
90°
SiRFP
SiRHP
B
SiRFP
SiRHP
charged
aliphatic
C
SiRHP's N-terminal topology
K73
Q72
L40
I1
h2
I2
I65
h4
R63
t1
h3
h1
b1
b2
N
b5
b12
b4
SiRHP's overall topology
c
N
b7
b8
siroheme
linker
h11
D
FMN
f-T404
f-H258
SiRFP
FNR domain
f-I247
f-Y498
h-K73
f-T248
h-Q72
f-F496
f-R250
f-V500
h-I65
h-L40
h-D38
h-R66
h-K127
h-D61
SiRHP
h-R63
h-F437
h-A443
Fe_4S_4
E
f-H258
h-K73
F
f-R250
h-I65
G
h-R63
h-F437

Figure 1: SiRFP and SiRHP interact through SiRFP's FNR domain and SiRHP's N-terminus. **A)** The SiRFP/SiRHP interface is minimal, governed by amino acids from three loops from SiRHP that fit into pockets on SiRFP's FNR domain. SiRFP's Fld domain is pink, SiRFP's FNR domain is light blue. SiRHP's N-terminal 80 amino acids are dark blue. SiRHP's core two S/NiRRs are green. **B)** The interface between the SiR subunits is governed primarily by hydrophobic interactions, in teal. Charged amino acids are gold and neutral amino acids are white. The subunits are displayed such that they are rotated 90° away from one another to show their interacting faces. **C)** The topology diagram of SiRHP, highlighting the N-terminal 80 amino acids whose structure was previously unknown but that govern the interactions with SiRFP. The amino acids that interact with SiRFP are localized to three loops. Hydrophobic amino acids are green, cationic amino acids are purple, and polar amino acids are yellow. The first S/NiRR is dark green whereas the second S/NiRR is light green, with the connecting h11 and linker in yellow and cyan, respectively ("Created with BioRender.com."). **D)** The interface between SiRFP and SiRHP is minimal. The SiRFP-FNR is light blue with light purple highlighted residues that are important for forming the SiRHP binding site. SiRHP'S N-terminal 80 amino acids are blue and the S/NiRR repeats are green with mauve highlighted residues that mediate the interaction with SiRFP. **E-G)** Select densities for important side chain interactions that mediate the interface between the SiRFP and SiRHP interface, colored as in **D**.

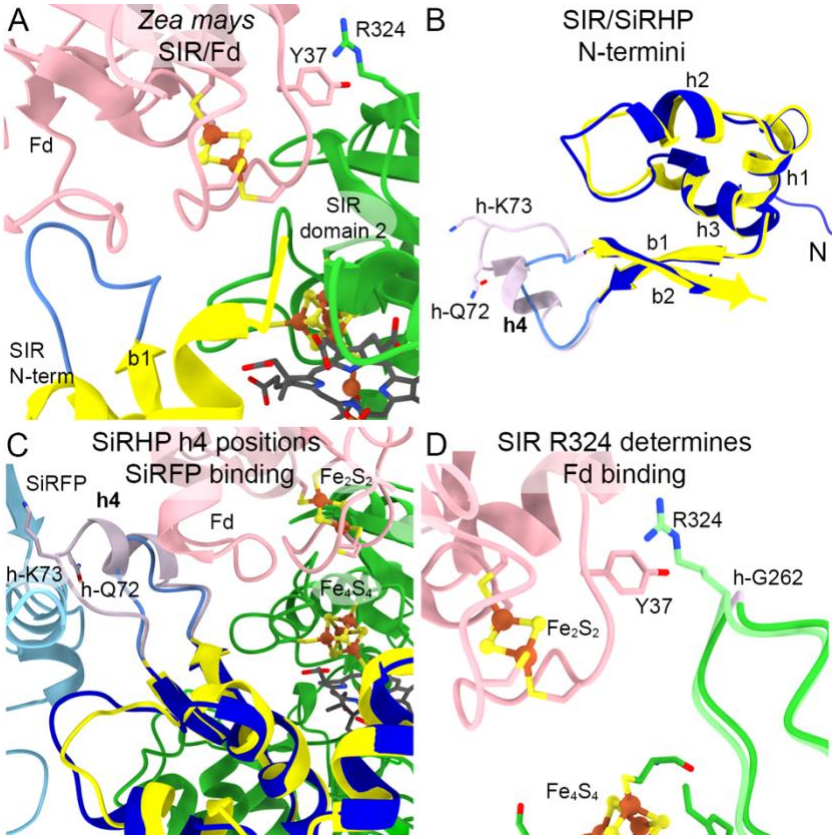

Figure 2: *Zea mays* SIR and *Escherichia coli* SiRHP interact with their reductase partners in different ways. **A)** SIR uses a ferredoxin (Fd, pink) as its reductase partner, which binds such that its Fe_2S_2 cluster is close to SIR's Fe_4S_4 cluster, positioned between SIR's N-terminus (yellow) and domain 2 (green). (PDB 5H92 (1)) **B)** SiRHP h4 (mauve) is the sole secondary structural feature that discriminates between SiRFP binding and Fd binding. SiRHP's N-terminal 80 amino acids are dark blue. SIR's N-terminal amino acids are yellow with the element equivalent to SiRHP h4 in medium blue. **C)** SiRFP (light blue) and Fd (pink) bind on different faces of SiRHP (dark blue) or SIR (yellow). Only the core S/NiRRs from SiRHP (green) are shown for clarity. Other elements are colored as in **B**. **D)** SIR R324 interacts with Fd Y37. That interaction is prevented in SiRHP because the position equivalent to SIR R324 is h-G262 (mauve).

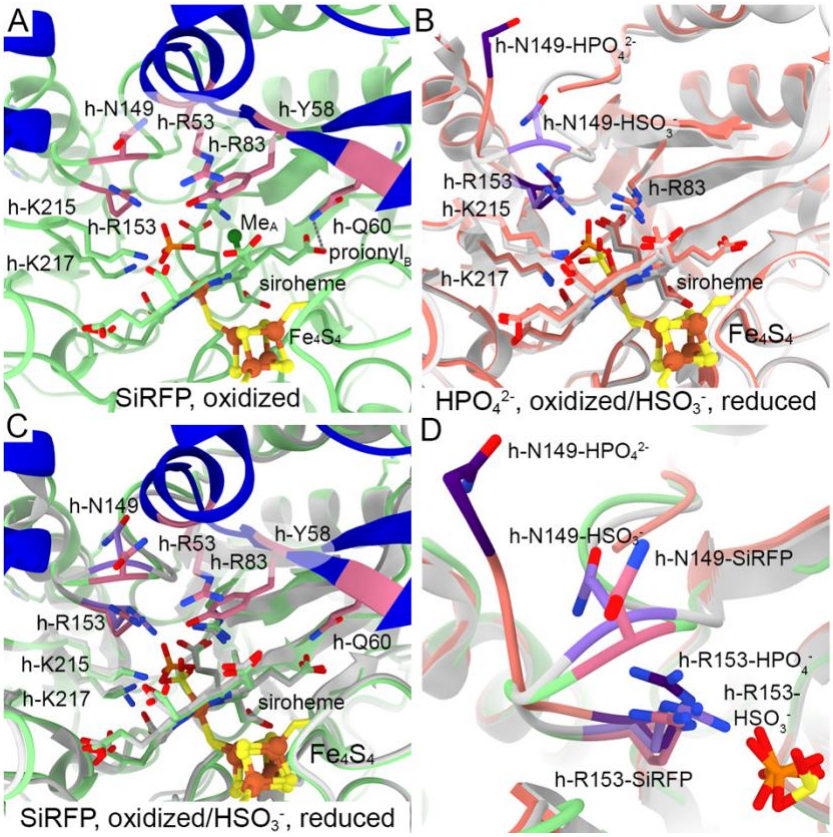

Figure 3: SiRHP's active site loop that forms the complete substrate binding site is in its closed conformation with the intact N-terminus, bound to SiRFP. Panels are labeled by their binding partner and oxidation state. **A)** When SiRFP binds oxidized SiRHP with the bound, inhibitory phosphate, the anion-binding loop containing h-N149 is ordered but with h-R153 in a similar orientation as in free SiRHP. Amino acids important for anion binding or loop position are dark pink. The siroheme methyl group from ring A is a dark green sphere and the interaction between h-Q60 and the ring B propionyl group is marked by a gray dash. **B)** In the absence of its N-terminal 80 amino acids, SiRFP, or the sulfite substrate, SiRHP's anion binding loop is disordered (pink ribbons). The amino acids that are important for anion binding in response to oxidation state or oxidase binding are dark purple (PDB 1AOP (2)). Upon reduction and with bound sulfite, the active site loop becomes ordered and h-R153 flips over to bind the substrate (light gray ribbons). The amino acids that are important for anion binding in response to oxidation state or oxidase binding are light purple (PDB 2GEP (3, 4)). **C)** Superimposition of the SiRFP-bound SiRHP (green) and the reduced, sulfite-bound, SiRHP (light gray) shows the anion-binding loop to be in similar position as in reduced SiRHP, primed for sulfite binding. **D)** Superimposition of the three SiRHP structures bound to different anions or binding partner highlights the intermediate conformation induced by SiRFP binding. This intermediate conformation shows ordering of SiRHP's N-terminus and the active site loop in a phosphate-bound, oxidized state. Models are colored as in **A-C**.

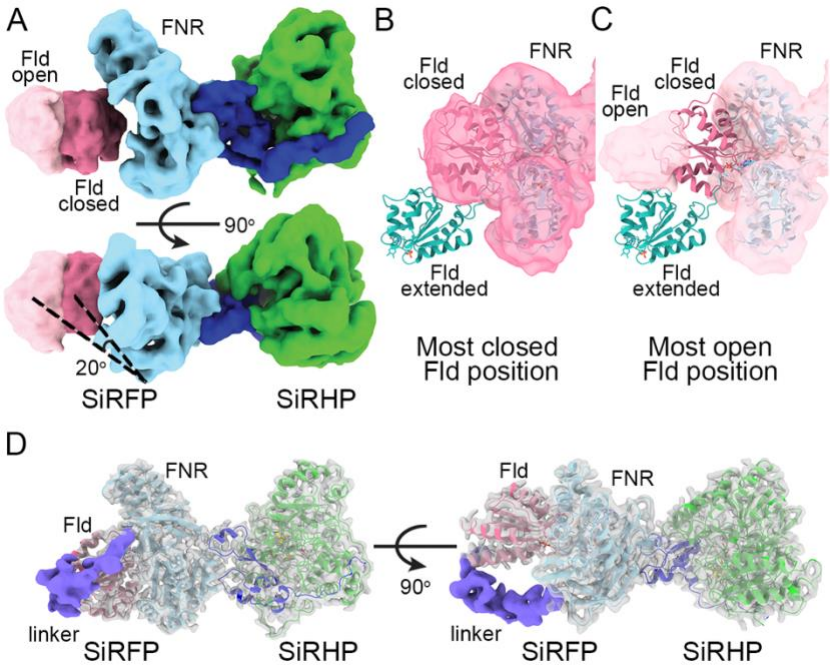

Figure 4: SiRFP's Fld domain is highly mobile relative to its FNR domain. **A)** One of the latent variable dimensions of motion demonstrates an opening of the Fld domain, even in SiRFP-60Δ, with the motion parallel to the midline of the FNR domain (light blue). The most-closed position is dark pink, the most open is light pink. SiRHP is green, with its N-terminus in dark blue. The angle is measured between the lines connecting the last traceable amino acid in the FNR domain with the open and closed Fld volume center of mass. **B)** The map of the most closed conformation of the Fld domain (dark pink) corresponds to the position of the Fld domain in the dimer formed with SiRFP-60X, far from where it is in the extended conformation of SiRFP-60Δ in crystals (teal, PDB 6EFV, (5)). **C)** The map of the most opened conformation (light pink) shows that the Fld domain lands in an intermediary position between a highly extended position seen in the X-ray crystal structure (teal, PDB 6EFV (5)) and the closed conformation seen in **B**. **D)** Even with the Fld and FNR domains constrained by a crosslink, the 36 amino acid-long linker between the domains is largely disordered, visible only in a small (~20,000) subset of particles (purple volume).

REFERENCES

1. J. Y. Kim, M. Nakayama, H. Toyota, G. Kurisu, T. Hase, Structural and mutational studies of an electron transfer complex of maize sulfite reductase and ferredoxin. *J Biochem* (2016).
2. B. R. Crane, L. M. Siegel, E. D. Getzoff, Sulfite reductase structure at 1.6 A: evolution and catalysis for reduction of inorganic anions. *Science* **270**, 59-67 (1995).
3. B. R. Crane, L. M. Siegel, E. D. Getzoff, Probing the catalytic mechanism of sulfite reductase by X-ray crystallography: structures of the Escherichia coli hemoprotein in complex with substrates, inhibitors, intermediates, and products. *Biochemistry* **36**, 12120-12137 (1997).
4. B. R. Crane, L. M. Siegel, E. D. Getzoff, Structures of the siroheme- and Fe4S4-containing active center of sulfite reductase in different states of oxidation: heme activation via reduction-gated exogenous ligand exchange. *Biochemistry* **36**, 12101-12119 (1997).
5. A. M. Tavolieri *et al.*, NADPH-dependent sulfite reductase flavoprotein adopts an extended conformation unique to this diflavin reductase. *J Struct Biol* (2019).